THE TIMBER GRID SHELL OF THE NEW ELEPHANT HOUSE AT THE ZOOLOGICAL-BOTANICAL GARDEN WILHELMA IN STUTTGART – INVESTIGATIONS ON JOINT STIFFNESSES AND CAPACITIES

DIE HOLZGITTERSCHALE DES NEUEN ELEFANTENHAUSES IM ZOOLOGISCH-BOTANISCHEN GARTEN WILHELMA IN STUTTGART- UNTERSUCHUNGEN ZUR STEIFIGKEIT UND TRAGFÄHIGKEIT DER KNOTENVERBINDUNGEN

Dominique Streib[1], Simon Aicher[1], Florian Gauss[2], Guillaume Caussarieu[2], Boris Peter[2]

[1] *Materials Testing Institute (MPA), University of Stuttgart, Otto-Graf-Institute*

[2] *knippershelbig GmbH, Stuttgart*

SUMMARY

The article reports on stiffness investigations of timber grid shell joints. The zoological-botanical garden in Stuttgart - also called Wilhelma - intends to build a new elephant house. For this purpose, a shallow timber grid shell construction has been chosen as the roof structure. For ultimate limit states and hereby especially the stability design of this shell, the stiffness of the node connections plays a decisive role. Full scale tests were designed and carried out to determine the joint stiffness behavior more precisely. The test results were then compared with calculations according to current design regulations.

ZUSAMMENFASSUNG

Der Beitrag berichtet über Steifigkeitsuntersuchungen von Holzgitterschalenknoten. Der zoologisch-botanische Garten in Stuttgart – auch Wilhelma genannt – beabsichtigt den Bau eines neuen Elefantenhauses. Als Dachkonstruktion ist eine flachgewölbte Holzgitterschalenkonstruktion geplant. Für die Standsicherheitsbemessung und insbesondere für die Stabilitätsbemessung dieser Schale spielt die Steifigkeit der Knotenverbindung eine entscheidende Rolle. Für eine genauere Ermittlung der Knotensteifigkeiten wurden vollmaßstäbliche Versuche konzipiert

und durchgeführt. Die Versuchsergebnisse wurden sodann den nach aktuellen Regelwerken rechnerisch ermittelten Steifigkeiten gegenübergestellt.

1.   INTRODUCTION

Shell structures often represent impressive wide-span load-bearing roof structures whose main objective is to create a wide-span and column-free space. The use of lightweight timber grid shells is especially tempting and rewarding compared to reinforced concrete shells due to sustainability assets. These are the lower CO_2 emission, during construction fostered by reduced foundation works and less material consumption in general and the CO_2 storage for the entire service life.

Examples of realized grid shells in timber construction are given hereafter. The cylindrical shell of the HanseMesse in Rostock, which was built in 2002, spans 65 m and is therefore considered one of the largest wooden lamella roofs. Also to be mentioned is the Multihalle in Mannheim with its different dome geometries. The exact shape of the grid shell built in 1975 was determined by an elaborate hanging model. The canopy in Dortmund, built in 1969, has the shape of a hyperbolic paraboloid. In order to prevent the occurrence of bending deformations during the assembly and service time, the edge was designed as a bending-resistant wooden rope [1].

In existing timber grid shell structures, frequently individual straight timber beams are used which are actively bent into their single or often double-curved shape [2]. In this case, special attention must be paid to the design of the edge connections, since the compressive forces increase at the supported periphery where the shell is less curved.

With shallow timber grid shells, the stiffness of the connections is particularly important. It controls the deflection of the shell as well as the design and lay-out of the edge connections. In softer systems, higher deflection occurs and the membrane load characteristics are endangered by locally occurring plate behavior. For stiff connections, the outer ring of the shell structure must be designed with regard to higher forces.

In the case of the elephant house, a relatively flat timber grid shell is conceived. The shell structure was modeled in a finite element program. The assignment of the stiffnesses in the numerical modelling plays a decisive role on the design of

the grid and rim connections. For this reason, elaborate experimental investigations were considered necessary to verify the actual stiffnesses in the grid shell nodes.

Fig. 1: Drawing of the elephant house © knippershelbig

2.   PROJECT DESCRIPTION

The state of Baden-Württemberg, represented by Vermögen & Bau Baden-Württemberg, Amt Stuttgart, intends to build a new elephant enclosure in the Wilhelma Zoo in Stuttgart. The architectural design is based on the first-placed competition entry by Hermann + Bosch Architects, MKK Architects and knippershelbig from 2017, see Fig. 1.

The maximum external dimensions of the building are approximately 100 m x 85 m. The building includes animal enclosures, visitor paths, a restaurant, stables and a shop with a partial basement. The enclosure area for the elephants is located at the centre of the main hall framed by single storey reinforced concrete structures. A dome-shaped timber lattice shell spans free over the centrally located hall. The dome's envelope is defined as a section of a torus surface which allows the use of quadrilateral planar insulated glazing units.

Fig. 2: Interieur view of new elephant house of Wilhelma Zoo
© Hermann+Bosch Architekten

The roof construction is designed as an arch structure with predominantly uniaxial load transfer. The loads from the individual arches in the primary direction (short span) are transferred directly into the concrete substructure via direct contact (Fig. 2). The secondary elements oriented in the secondary direction(s) are used for load distribution and stabilization of the shell structure. A triangular concrete beam is integrated into the horizontal concrete ceiling slab, running along the oval shaped roof opening and transfers the support forces of the timber shell into the adjacent columns and walls (see Fig. 3).
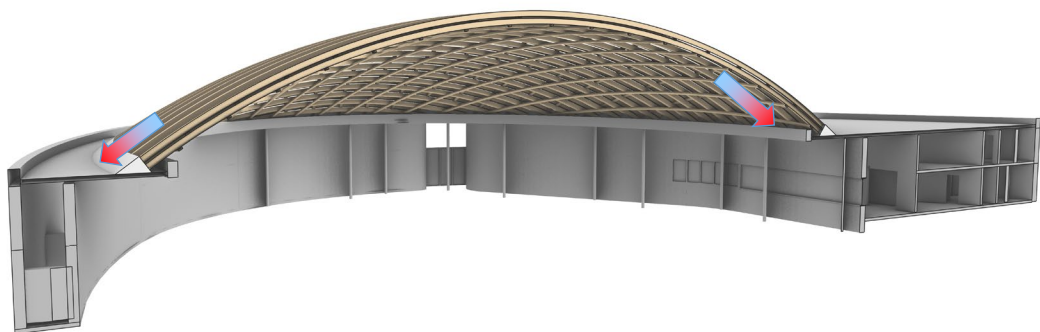
Fig. 3: Isometric view of grid shell arch structure of elephant house © knippershelbig
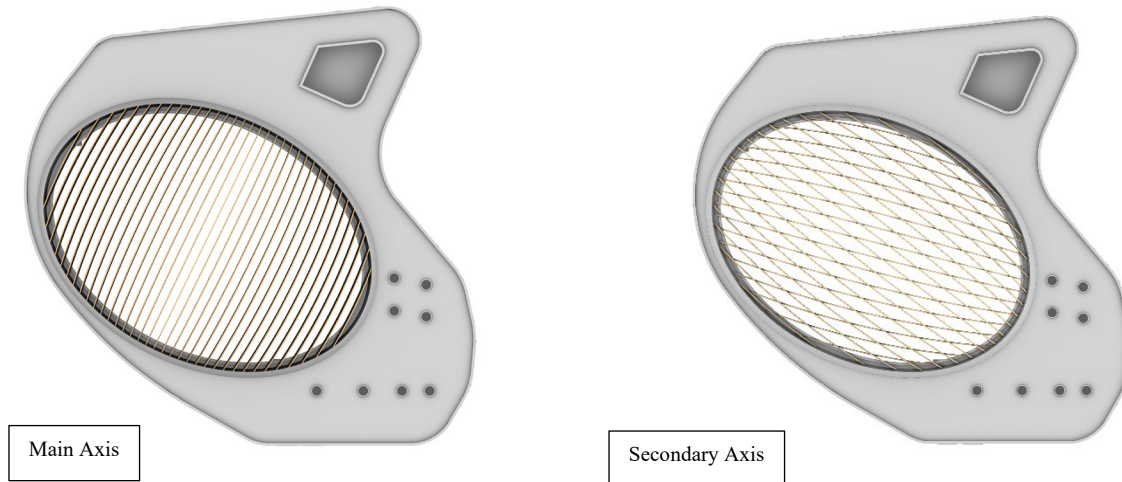
Fig. 4: Major load paths of elephant house grid shell structure © knippershelbig

The three-axis carrier network is composed of four layers of glulam timber (GLT) sections. The GLT members of strength class GL28h in layers one and three (starting from the top) each with cross-sectional dimensions width x height = W x H = 24 cm x 32 cm are forming the main arches. The members in layers two and four are orientated in the secondary direction(s). They consist of GL28h, too and show dimensions W x H = 24 cm x12 cm. These members are running diagonally to set the space between the main double arches and to provide lateral stability. The layered build-up of the lattice allows node details which only require the transfer of forces between two members at one shear plane. The two diagonal layers intentionally do not intersect at the same point to decompose the force transfer into individual shear planes.
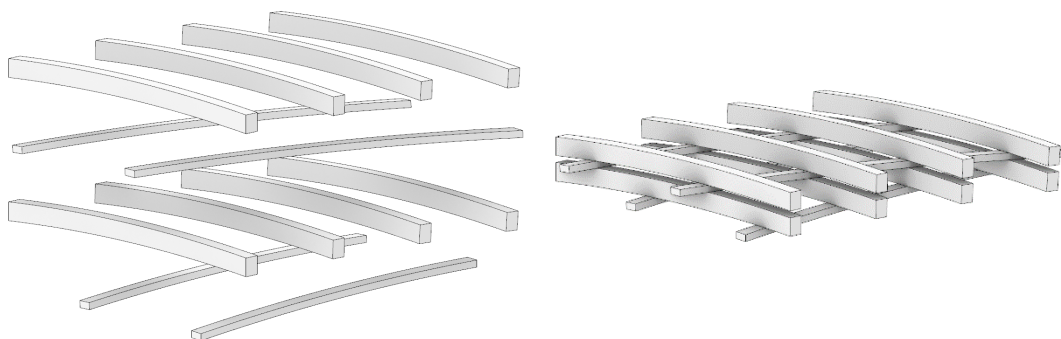
Fig. 5: Isometric explosion view of four-layered timber lattice grid shell roof structure
© knippershelbig

A simple node detail was developed using split ring connectors for the shear transfer and additional long fully-threaded self-tapping screws to resist against the accruing moments in the connection (see Fig. 6).
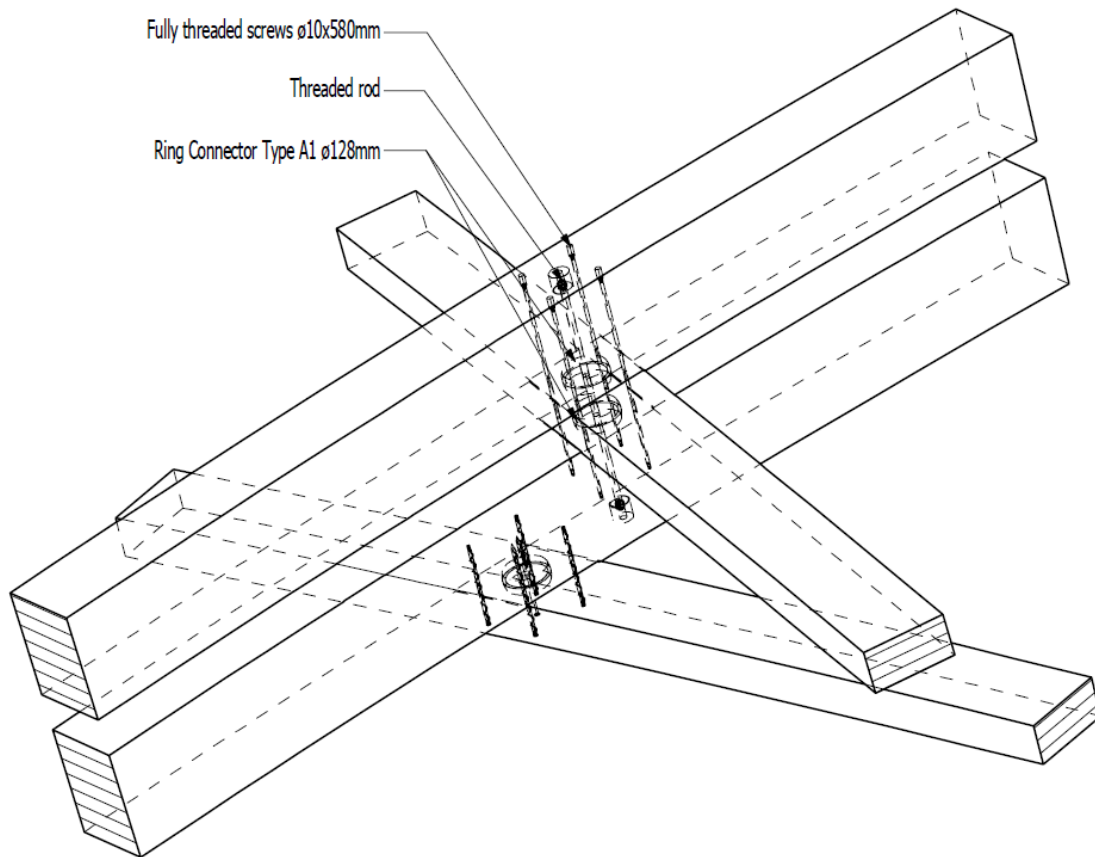
Fig. 6: Isometric view of grid shell node detail © knippershelbig

The internal forces at the grid shell nodes, in particular the connection of the two transverse beams and the diagonal in between, are largely determined by the stiffness of this connection. This stiffness results from the interaction of the fasteners (split ring connectors and screws) and from the shear stiffness of the diagonals themselves. The effective stiffness can be estimated by analytical methods only in approximate manner. Hence, the actual design internal forces acting on the node can only be determined by tests with sufficient accuracy then enabling a realistic design. Determining the correct stiffness and validating the load-bearing capacity of the cross node are essential components of the entire static calculation of the roof structure. The tests and the respective evaluations were performed at MPA University of Stuttgart, Department of Timber Construction in close cooperation with knippershelbig GmbH.

The roof structure is processed as an engineering structure in an agile, interdisciplinary and iterative planning process. A clear assignment of the parametric digital planning method to the Official Scale of Fees for Services by Architects and Engineers (HOAI) service phases is not possible. Partial services of work phases 2-5 are performed several times in different iterations and refined with each run. For example, two different three-dimensional geometry and calculation models are already required at the beginning of the performance phase to find a solution, or detailed control concepts and construction processes are already reassessed in the preliminary planning. The geometry is determined with a high degree of accuracy (several decimal places) right from the start, only the level of detail is increased in each planning phase.

To achieve the highest quality level during execution the Swiss-based company "Design to Production (D2P)" was integrated into the design team right from the beginning of the project. D2P are specialists in digital design and manufacturing processes of timber structures. The design of the timber components is set out as a continuous process chain from planning to CNC production and construction. The seamless digital process is ready for execution as the digital data is used directly for the joinery of the timber construction elements in coordination with a potential executing company in timber construction (after the tender) was established. In terms of quality assurance and digital planning, the project is taking on a pilot character for the state of Baden-Württemberg.

3.   STIFFNESS TESTS ON GRID SHELL NODES

3.1   Test program and Layout

Fig. 7 shows the nodal connection including the coordinate system. In order to estimate the stiffnesses of the joint, four test series with different test configurations were performed.

For the design of the structure, the determination of the joint stiffness is relevant for four degrees of freedom. For this reason, two shear stiffness test series and two bending rotation test series aiming at rotational stiffness were conceived with cross-section wise full-scale joint specimens:

- shear tests in the direction of the girders (K_{Fx})
- shear tests in the direction of the diagonal (K_{Fy})

- bending rotation tests about the y-axis (K_{My})

- bending rotation tests about the x-axis (K_{Mx}).

In addition to the nodal stiffness determination also the load-bearing capacity of the connection was determined in three of the four tests.

Following two test series, i.e. the shear tests in axial direction of the girders and the bending rotation tests about the y-axis, are described in more detail. The results of all experiments are presented, too.
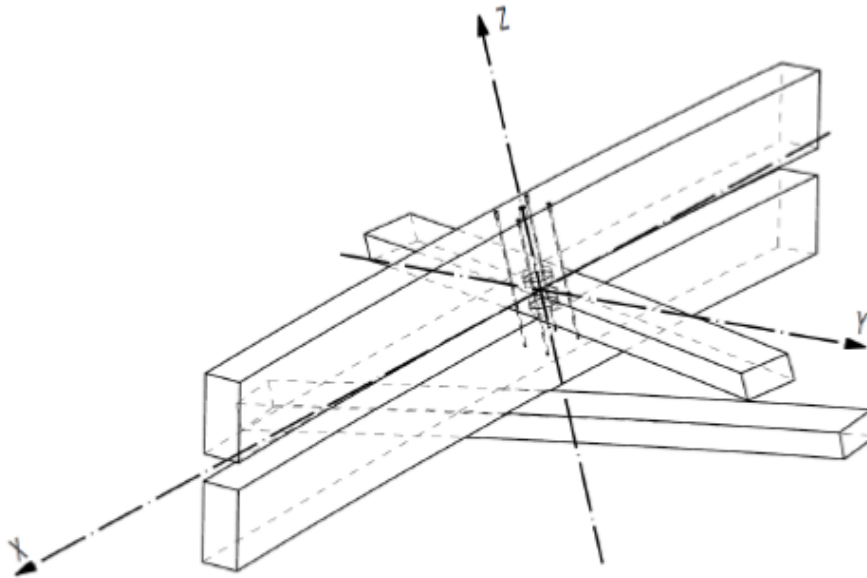
Fig. 7: Local node axes © knippershelbig

3.2   Specimen description

A specimen consists of two parallel GLT main girders and an internal GLT diagonal, which runs at an angle of 78.5° to the longitudinal girder axes. The GLT girders each have dimensions of 240 mm x 320 mm and a length of 1500 mm. The diagonal has a cross-section of 240 mm x 120 mm and a length of 1000 mm. The beams are connected to each other with split ring connectors of Type A (EN 1995-1-1:2004 [3]) with a diameter of Ø 128 mm. Additionally there are an internal threaded bolt Ø 16 mm as well as four fully-threaded self-tapping screws with a diameter of Ø 10 mm, which are arranged symmetrically around the split ring connectors and have an embedment length in the upper and lower girders of 200 mm and 210 mm, respectively. In total 15 grid shell nodes of the roof structure of the new elephant house were tested at MPA.

In order to evaluate the stiffness test results as realistic as possible, the effective densities of all GLT specimens were determined. The mean density involved as: $\rho_{test} = 412 \pm 21$ kg/m³ ($COV = 5{,}2$ %).

3.3   Shear tests in the direction of the girders (K_{Fx})

The shear tests were closely aligned with the specifications in EN 408 [4] and EN 789 [5]. The shear forces are mainly absorbed by the split ring connection. The test specimens were beveled at an angle of 18.1° at the end-grain surfaces of the girders and installed in the test machine in such manner that the load application point at the top chord and the support point on the bottom chord are positioned vertically in coinciding with the piston dictated load axis. Consequently, no load eccentricity occurs.

A schematic view of the test setup of the shear tests parallel to the girders is shown in Fig. 8. Figs. 9 a and b show the realized test setup.

To determine the relative displacement between the girders and the internal diagonals, two deformation sensors (LVDt) based on the electrical resistance principle were attached to each shear plane. The positions of the displacement sensors as well as the (sub-) joint identification are shown in Fig. 8. Thus, the deformations are measured separately for both shear planes, also called (sub-) joints.

The shear tests were performed path-controlled in a servo-hydraulic, computer-controlled test machine in a heated (20°C ± 2°C), yet not acclimatized test hall. In order to determine the shear stiffness of the node connection in x-direction within the elastic, quasi-plastic and damage loads regimes, several subsequent load cycles according to EN 26891 [6] were applied to each specimen. A constant cross-load speed of 2.0 mm/min was applied up to a specified force (after every load cycle the load was increased). The force was then kept constant for 10 seconds and hereinafter reduced to 1.0 kN at the same test speed to keep it constant again for 10 seconds.

After achievement of further predetermined load cycles the tests were finished in a path-controlled manner at a constant test speed of 4.0 mm/min until the respective failure load was reached. The first specimen was loaded as described above in several loading cycles up to 30 %, 40 % and 50 % of a previously estimated maximum load. In the follow-up tests, the load cycles were then adjusted to the result of the first specimen.
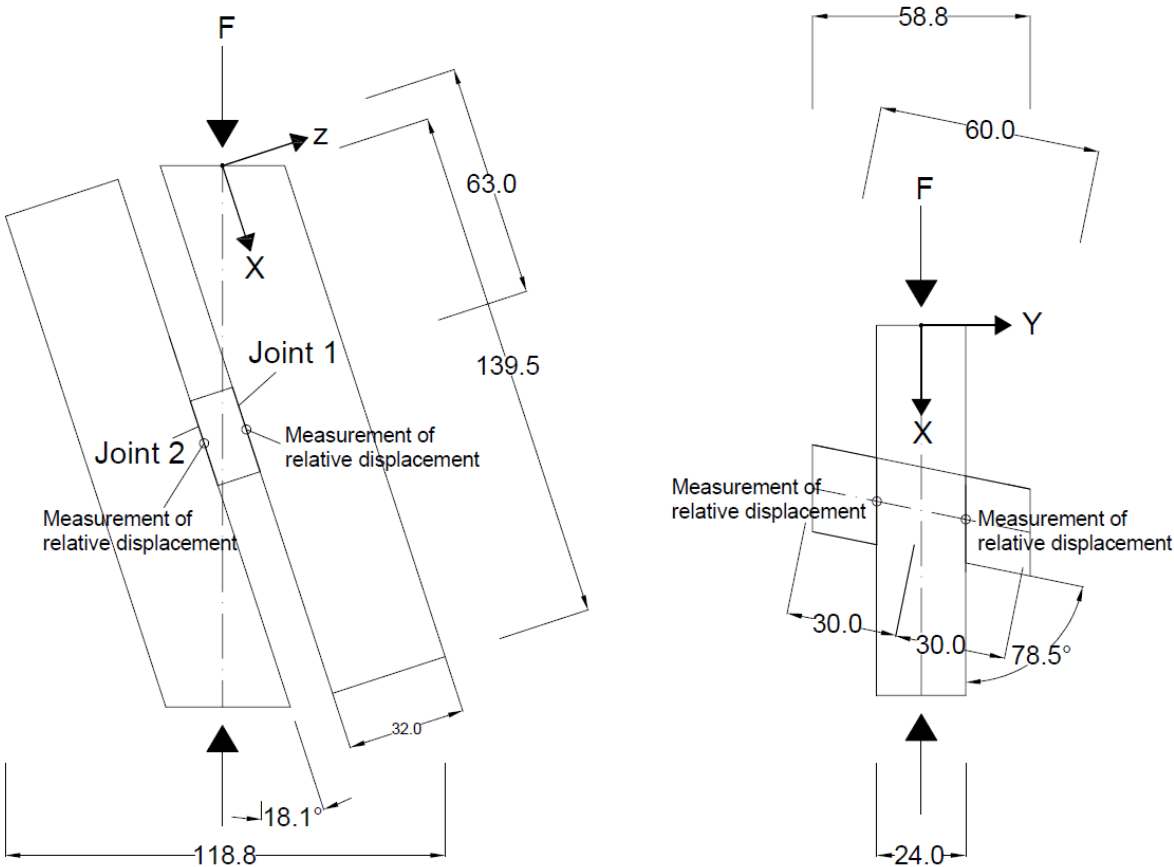
Fig. 8: Schematic test setup for determination of K_{Fx} stiffness (shear in axial (x) direction of the girders); Dimensions in cm

a)   b)
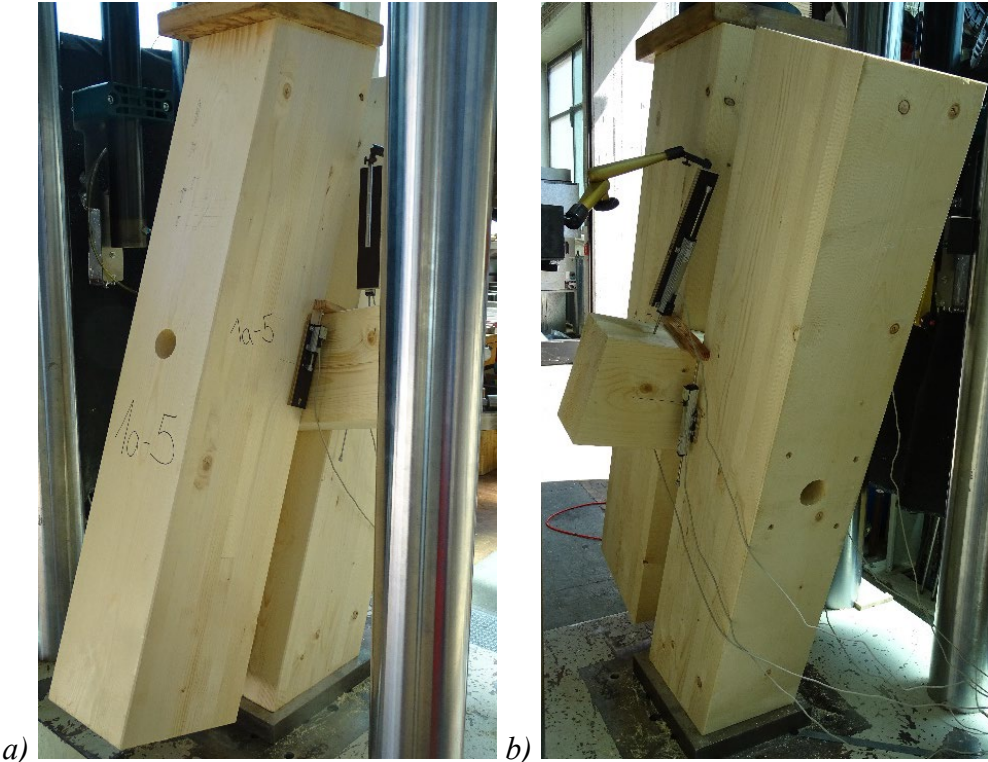
Fig. 9: Realized test setup of K_{Fx} stiffness tests

3.4 Bending tests about the y-axis (K_{My})

A schematic view of the test set-up is shown in Fig. 10. The realized test configuration is depicted in Fig. 11. For the bending tests about the y-axis, EN 26891 [6] was applied as a loading method. At a distance of 700 mm from the center of the grid shell node, the upper chord was loaded by a point load, while the lower chord on the other side of the grid node was clamped to the horizontal beam of the test machine with a type of caliper fastening. The shear force and moment applied to the upper beam is counteracted by tensile and compressive forces in the joints. The tensile force is in first instance, i.e. disregarding stiffness friction effects from the rotating split ring connector, exerted entirely via the fully threaded screws. In the case of compressive loading, the force is additionally transmitted via contact between the chord and the diagonal. To measure the cleavage and indentation displacements related to these tension and compression components, four displacement sensors were attached to each joint and placed at the axis of the screw pairs. The rotation of the upper beam vs. the lower rigidly fixed member was measured by additional LVDTs mounted at 250 mm distance from the diagonal as shown in Fig. 11. The position of the displacement sensors and the numbering of the two joints are given in Fig. 10.

The bending tests were conducted in displacement control with a constant piston speed of the employed servo-hydraulic, computer-controlled test machine. In order to determine the rotational stiffness of the node about the strong direction of the girders, several load cycles were applied to each specimen. The individual limits of the load cycles were selected as for the shear test. The first specimen was loaded in several loading cycles of about 50 %, 70 %, 90 % and 100 % of a previously estimated maximum load. In the follow-up tests, the load cycles were then adjusted to the result of the first specimen.
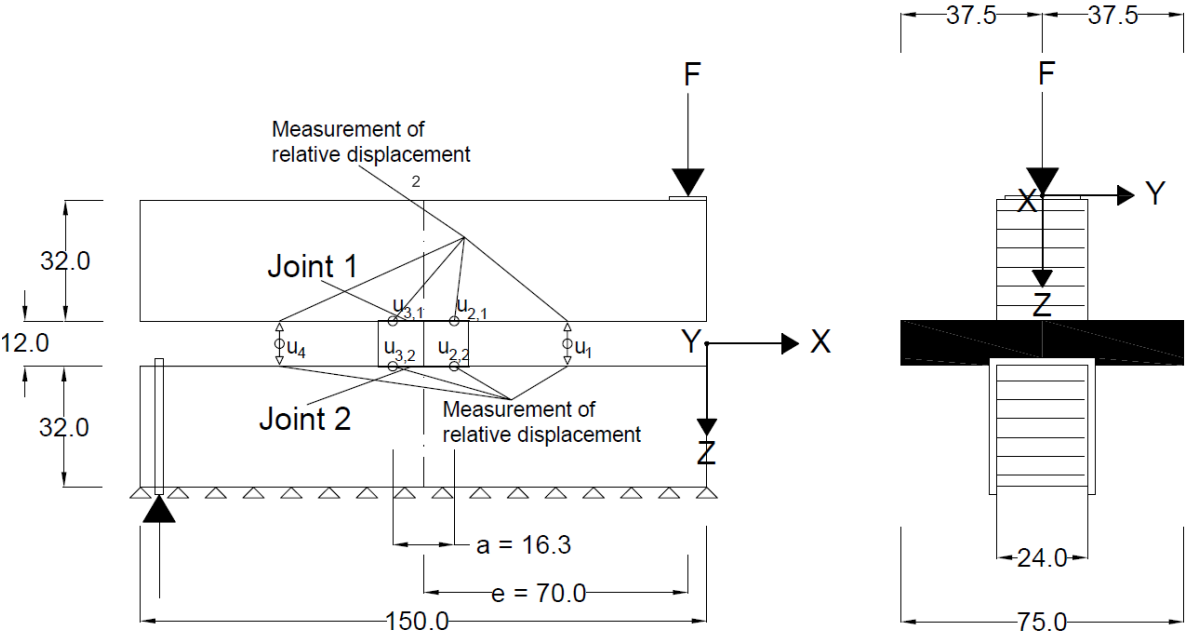
Fig. 10: Scheme of test setup for determination of K_{My} stiffness (= bending about the y-axis); Dimensions in cm

Fig. 11: View of realized test setup for determination of K_{My} stiffness (= bending about the y-axis)

The rotational stiffness was calculated from:

$$K_\varphi = \frac{M}{\varphi} \tag{1}$$

$$\varphi = \frac{u_2 + u_3}{a} \ , \ \ M = F \cdot e \tag{2), (3}$$

where M is the bending moment determined by the distance e = 700 mm between the load axis and the center of the grid shell node. The angle of rotation φ is based on the measured relative displacements. For this purpose, the measured displacements u_2 and u_3 of the two opposite displacement sensors at both sides of the beams were averaged for each plane for the tension as well as the compression side of the joint. The distance between the tension and compression components was a= 163 mm.

4.   TEST RESULTS

4.1   Shear tests in the direction of the girders (K_{Fx})

For all five specimens, a stiffness was determined for shear plane 1 and 2 (see Fig. 8). The stiffness was calculated in accordance with EN 408 [4]. In order to obtain an approximately linear-elastic range in the load-deformation curve, the upper and lower load values for the stiffness determination were precisely adjusted for each specimen and shear plane. Thereby, the correlation coefficients for the slope determination were consulted. Thus, lower load values of 10 % to 23 % and upper load values of 41 % to 53 % were obtained.

For the determination of the stiffness, the measured displacements of the two opposite displacement sensors on both sides of the joint were averaged for each shear plane. A representative load-deformation diagram of the specimen No. 1a-01 is shown as an example in Fig. 12. After each loading cycle, the connection of the timber grid shell node showed a very pronounced increase in remaining plastic deformation. In the descending and subsequently increasing load path of each load cycle, the curves are rather vertically aligned. The nodal connection appears to deform minimally during load decrease where a relatively stiff behavior van be seen. Only after the previous maximum load is reached the load-deformation diagram resumes its slope, which is relevant for the stiffness determination. To illustrate this, an equivalent curve ("stiffness curve") was determined for each shear plane.
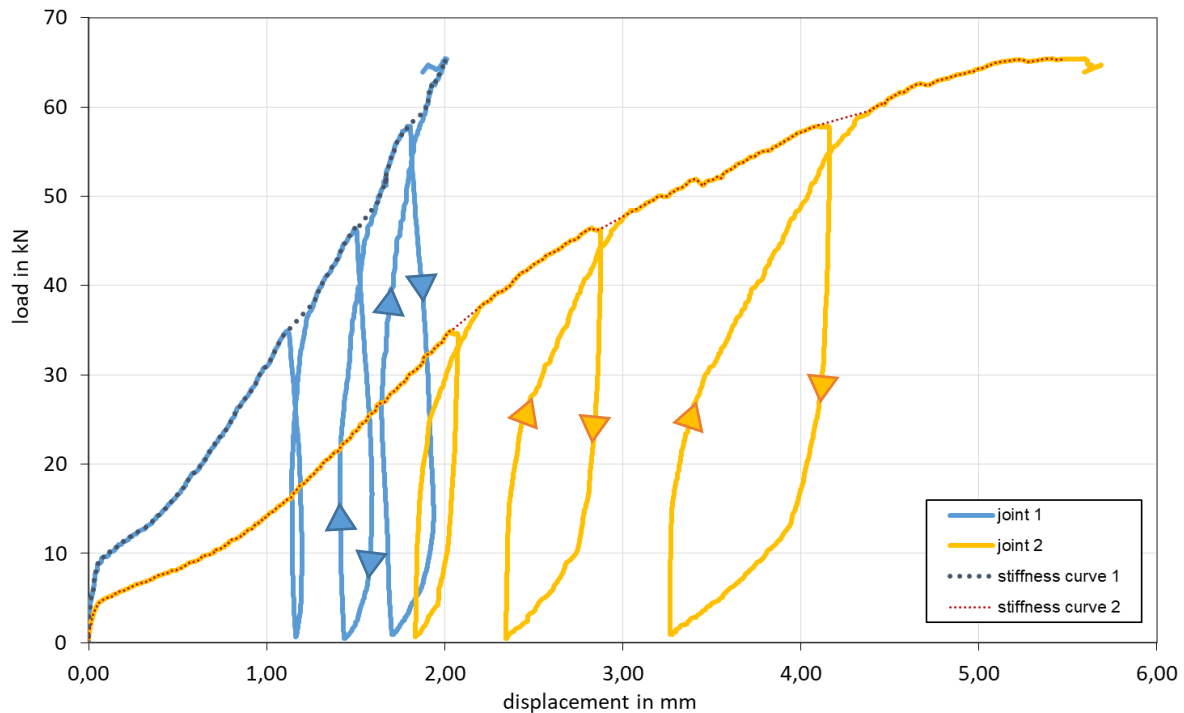
Fig. 12: Load deformation diagram of specimen No. 1a-01

After the first loading cycle, the plastic deformation is visible by a minor indentation of the diagonal in the girders. During the last loading cycle, splitting fractures in the diagonal became apparent, which continued to grow even after the maximum load had been reached. The tests were stopped in consequence of the large deformations. Figs. 13 a and b show test specimen No. 1a-02 after termination of loading. The results for the stiffness parameter K_{Fx} deduced from the test results are given in chapter 5.

a)   b)

Fig. 13: Typical fracture appearance (here specimen 1a-02) with crack formation in the diagonal

4.2 Bending tests about the y-axis (K_{My})

Figs. 14 and 15 show the load-deformation diagrams exemplary for specimen No. 1b-03 with the deformations u_2 as the compression and u_3 as the tensile component, respectively. The four load cycles 1b-03-1 to 1b-03-4 are clearly identifiable by the loop shape.

Based on Equations (1-3) and the depicted displacements, Figs. 16 and 17 show the rotational stiffnesses as dependent on the applied load. The individual curves represent the results of the four load cycles reaching up to 50 %, 70 %, 90 % and 100 % of ultimate load. The curves relate to the load range between 10 % and 40 % of the respective fracture load; an exception hereof is the first load cycle where the curve ends before 40% of the fracture load.
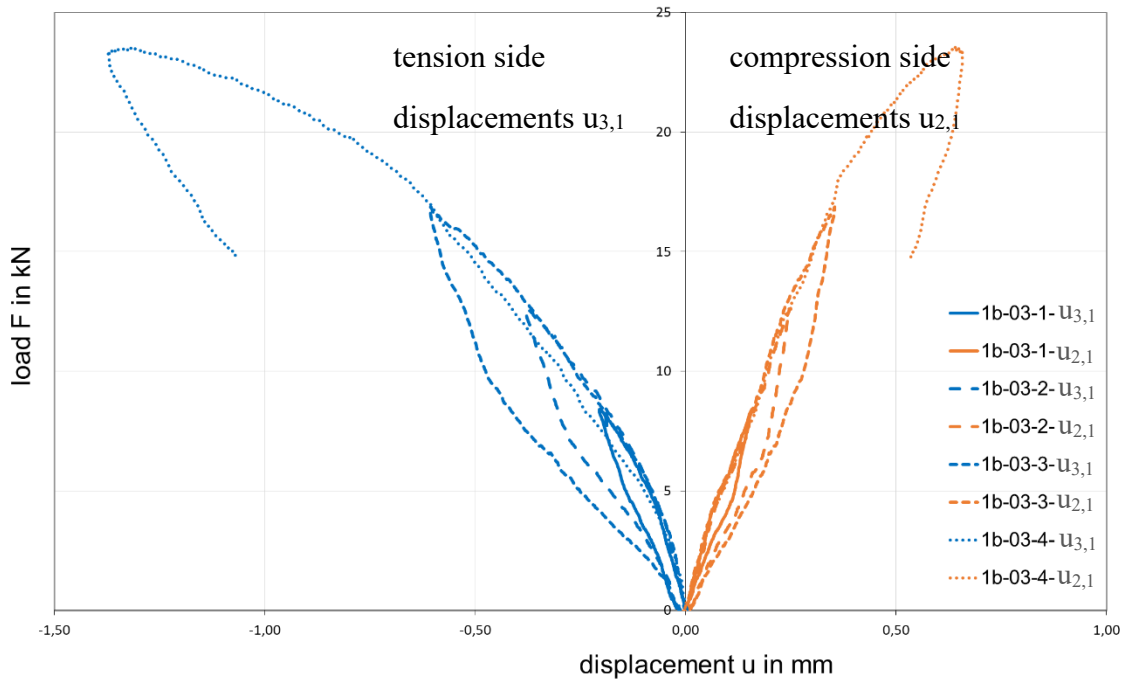
*Fig. 14: Typical load deformation diagrams for u₂,₁ and u₃,₁ (here: specimen No. 1b-03; **joint 1)***
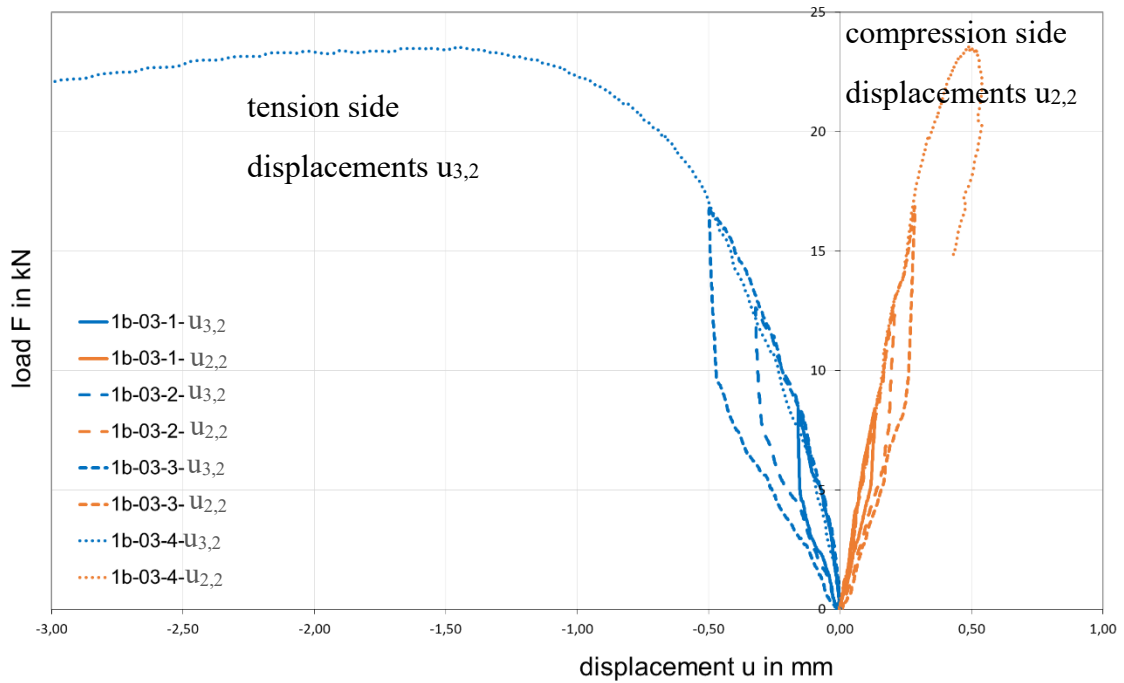
*Fig. 15: Typical load deformation diagrams for u₂,₂ and u₃,₂ (here: specimen No. 1b-03; **joint 2)***
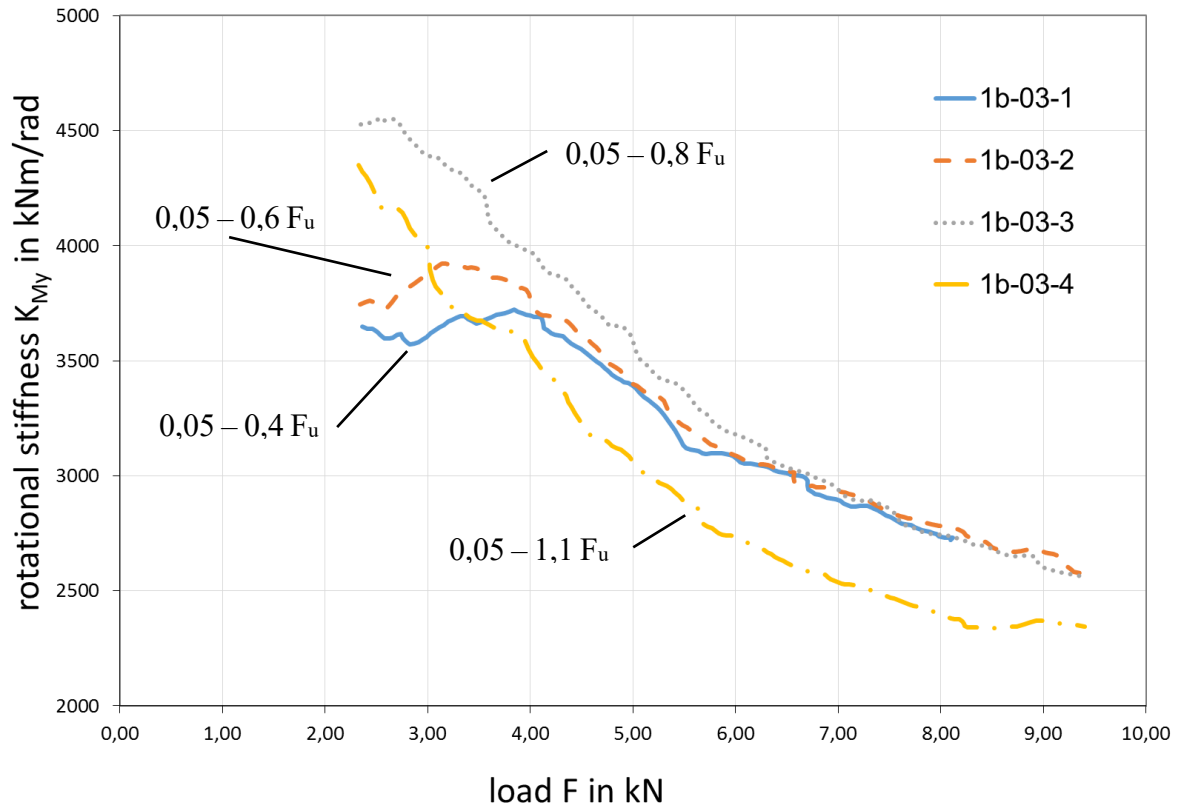
*Fig. 16: Rotational stiffness over load for all load cycles (here: specimen No. 1b-03; **joint 1**)*
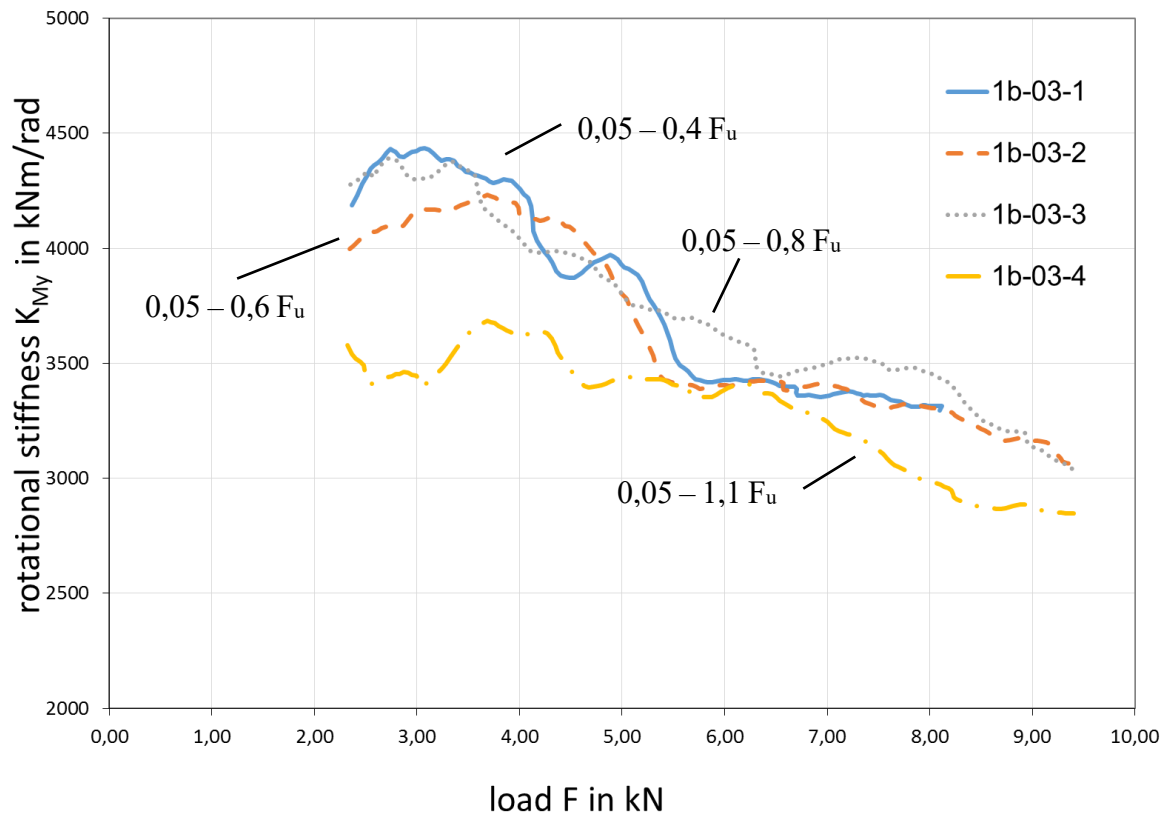
*Fig. 17: Rotational stiffness over load for all load cycles (here: specimen 1b-03; **joint 2**)*

It is apparent from Figs. 16 and 17 that the rotational stiffness decreases almost linearly with increasing load during a cycle. Furthermore, for two test specimens (1b-04 and 1b-05) it could be observed that the rotational stiffness decreases with increasing number of load cycles. Even for specimen 1b-03, the last one i.e. the ultimate load cycle exhibits the lowest rotational stiffness on average compared to the previous loading cycles.

Within the first two load cycles, i.e. up to 0.7 F_u, a purely elastic behavior of the nodal connection can be observed. Only at a load of 80 % of the maximum load the deformation sensors of the tensile components show a pronounced nonlinear behavior. Approaching the maximum load, the upper chord becomes visibly inclined (see Fig. 18). A gap with pulled-out screws gets visible between the diagonal and the bottom chord. The center bolt Ø 16 mm has bent significantly in such a way that it could not be removed from the specimen after the test. Figs. 18 and 19 show the test specimens with the respective failure images.
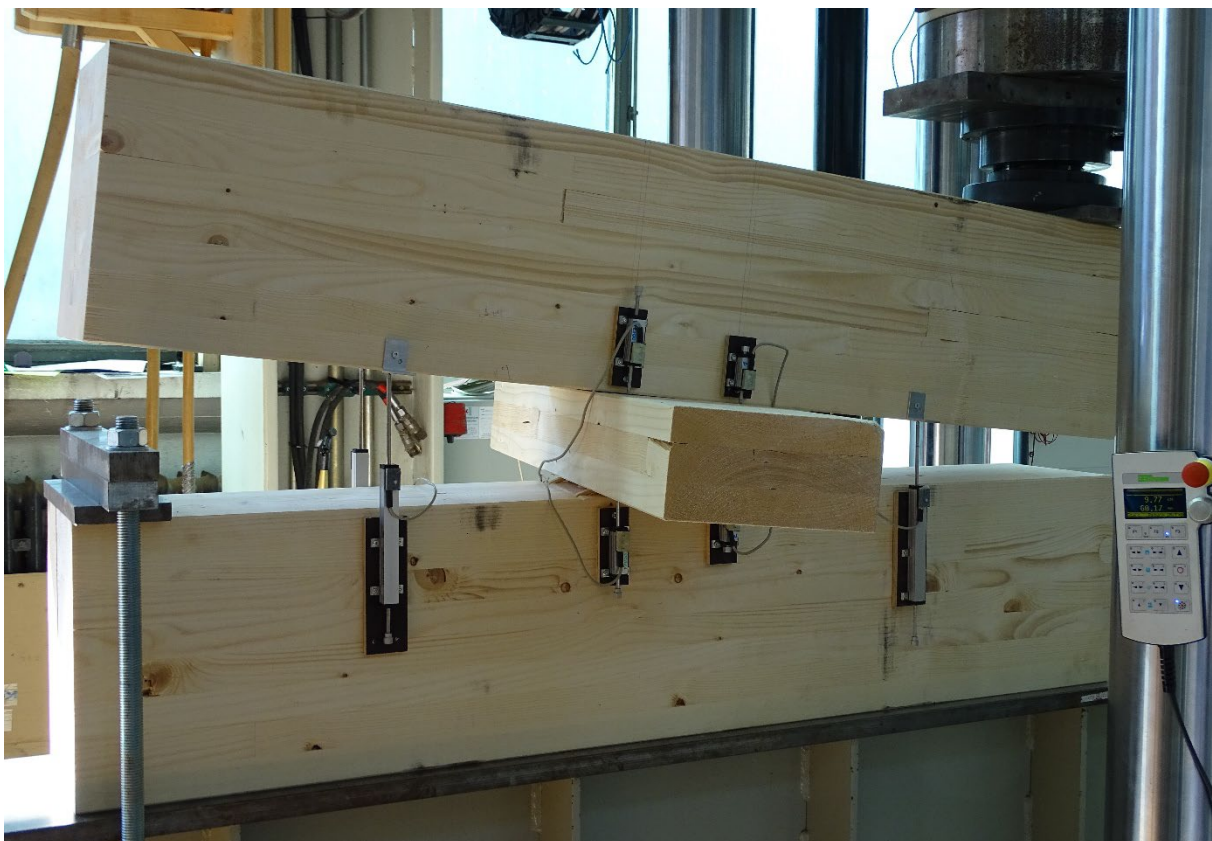
Fig. 18: Failure image using specimen 1b-01 as an example; inclination of the top chord

Fig. 19: Typical failure appearance in the bending tests (here specimen 1b-01); the pull-out of the screws between diagonal and bottom chord

It seems sensible that the central bolt Ø 16 mm contribute to the rotational stiffness and load-bearing capacity of the entire connection. In order to verify this assumption, the bolt was removed at specimen 1b-05 before testing. Indeed, the last cycle of specimen 1b-05 showed the lowest rotational stiffness of all five moment specimens. In addition, the achieved failure load $F_{max,\ 1b-05}$ =20.91 kN represents the lowest value of all test specimens, although the difference to the average failure load of the other specimens is only 10 %.

5.   STATISTICAL EVALUATION OF THE TEST RESULTS

The statistical evaluation for the tests was performed according to EN 14358 [7]. The characteristic 5 % quantile value of the maximum load was derived on the assumption of a lognormal distribution. The characteristic values of the different stiffnesses were determined as the characteristic mean value m_{mean} according to Section 3.3 e) in [7].

Table 1: Results of shear tests in the direction of the girders ($F_{x,max}$ and K_{Fx})

	Maximum load $F_{x,max}$ [kN]	shear stiffness $K_{F_{x,1}}$ joint 1 [kN/mm]	shear stiffness $K_{F_{x,2}}$ joint 2 [kN/mm]
Number of specimens	5	5	5
Mean value	73.0	25.21	21.99
Standard deviation	7.07	5.31	3.93
Coefficient of variation	9.7 %	21.1 %	17.9 %
Minimum value	65.4	19.87	17.58
Characteristic value according to EN 14358	57.3	23.45	20.69

Table 2: Results for shear tests in the direction of the diagonal ($F_{y,max}$ and K_{Fy})

	Maximum load $F_{y,max}$ [kN]	shear stiffness K_{F_y} both joints [kN/mm]
Number of specimens	5	27
Mean value	289	58.4
Standard deviation	18	13.8
Coefficient of variation	6.2 %	23.6 %
Minimum value	270.5	29.2
Characteristic value according to EN 14358	247.5	56.6

Table 3: Results for bending tests about the y-axis ($F_{y,max}$ and K_{My})

	Maximum load $F_{y,max}$ [kN]	Rotational stiffness upper joint $K_{M_{y,1}}$ [kNm/rad]	Rotational stiffness lower joint $K_{M_{y,2}}$ [kNm/rad]
Number of specimens	5	22	22
Mean value	22.8	3251.7	4044.8
Standard deviation	1.45	359.5	822.3
Coefficient of variation	6.4 %	11.1 %	20.3 %
Minimum value	20.9	2138.5	2449.4
Characteristic value according to EN 14358	19.4	3197.2	3920.1

Table 4: Results for bending tests about the x-axis (K_{Mx})

	Rotational stiffness joint 1 $K_{M_{x,1}}$ [kNm/rad]	Rotational stiffness joint 2 $K_{M_{x,2}}$ [kNm/rad]
Number of specimens	16	16
Mean value	3167	1868
Standard deviation	895	219
Coefficient of variation	28.3 %	11.7 %
Minimum value	1947	1599
Characteristic value according to EN 14358	3006	1829

6. ANALYTICAL DETERMINATION OF THE STIFFNESSES

6.1 General

Apart from the experimental determination of the regarded connections in the different load directions these can also be determined analytically. The necessary, more or less rough respective assumptions and a comparison with the test results are given in this chapter.

6.2 Shear stiffness in x-direction of the connection

The slip modulus of a split ring connector (Type A) is specified in EN 1995-1-1:2004 [3], Chapter 7, as

$$K_{ser} = \frac{\rho_m d_c}{2} \tag{4}$$

where

ρ_m mean density of the timber

d_c connector diameter

The mean density of the employed GLT strength class GL 28h is given in EN 14080 as $\rho_m = 460$ kg/m³. This value is 12 % higher as the mean density derived from the test specimens ($\rho_{m,test} = 412$ kg/m³).

The slip modulus K_{ser} according to Eq. (4) results in ($d_c = 128$mm)

$$K_{ser,\rho_{nom}} = \frac{460\frac{kg}{m^3} \cdot 128 \text{ mm}}{2} = 29440 \ \frac{N}{mm}, \tag{4a}$$

$$K_{ser,\rho_{test}} = 26368 \ \frac{N}{mm}. \tag{4b}$$

In addition to the slip contribution of the split ring connector, the shear distortion of the diagonal should also be taken into consideration and accounted for the determination of the joint stiffness. For the stiffness determination in x-direction, it has to be recalled that the girders and the diagonal in between are not crossing at an angle of 90° but at an angle of 78.5° (see Fig. 8). In order to evaluate the shear rigidity of the diagonal in x-direction correctly, shear modulus $G_{78.5°}$ has to be determined, which sensibly should be higher as compared to the pure rolling shear modulus G_{90} which can be assumed as 65 N/mm² (which is 10 % of $G_0 = 650$ N/mm²). In order to assess the angle influence in a rough approach the Hankinson equation [8] is used which is generally applied for determination off-axis stresses ($\sigma_\alpha = \sigma_0 \cdot \sigma_{90} / (\sigma_0 \cdot sin^2\alpha + \sigma_{90} \cdot cos^2\alpha)$), hence

$$G_\alpha = \frac{G_0 \cdot G_{90}}{G_0 \cdot sin^2\alpha + G_{90} \cdot cos^2\alpha} \tag{5}$$

Inserting G_0, G_{90} and $\alpha = 78.5°$, one obtains

$$G_{78,5°} = \frac{650\frac{N}{mm^2}·65\frac{N}{mm^2}}{650\frac{N}{mm^2}·\sin^2 78.5°+65\frac{N}{mm^2}·\cos^2 78,5°} = 67 \ \frac{N}{mm^2}. \tag{5a}$$

It is appearent that the slight deviation from an orthogonal crossing of the girders and the diagonal has an almost negligible influence on the "rolling shear modulus".

The shear distortion of the GLT cross section is proportional to the applied shear force T and inversely proportional to the shear stiffness (see also Fig. 20).
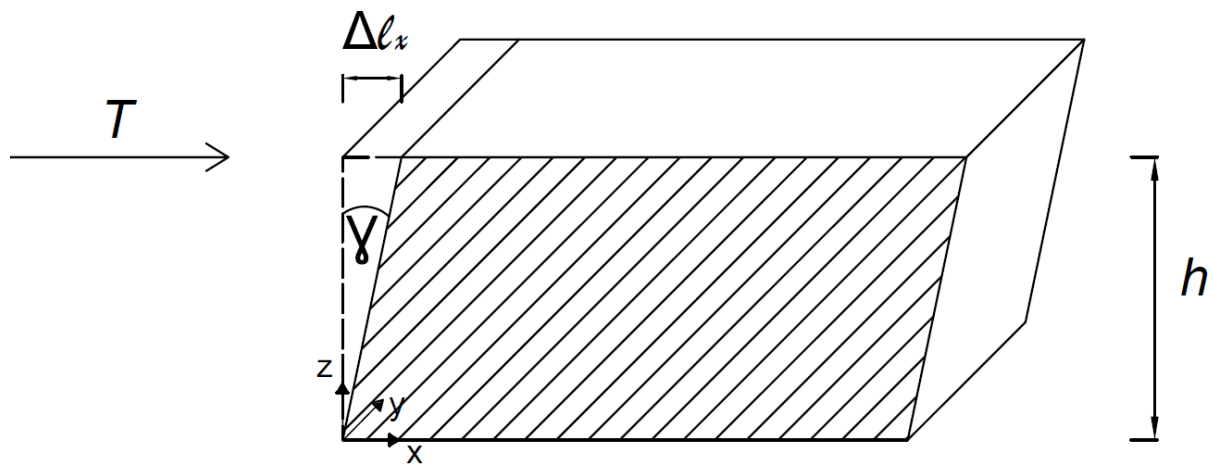
Fig. 20: Illustration of the shear distortion of the diagonal in between of the two adjacent girders

$$\gamma = \frac{T}{G·A_s} = \frac{T}{G·A} \tag{6}$$

With the geometric conditions and the approach for small angles, the distortion length Δl_x is obtained as

$$\Delta l_x = h · \gamma . \tag{7}$$

Combining Eqs. (6) and (7), the shear rigidity results in

$$K_{x,diagonal} = \frac{T}{\Delta l_x} = \frac{G·A}{h} = \frac{67\frac{N}{mm^2}·240\ mm·240\ mm}{60\ mm} = 64320 \ \frac{N}{mm}. \tag{8}$$

The combined effect of the shear stiffnesses of the split ring connector and of the GLT shear rigidity is then determined on the basis of a series coupling as
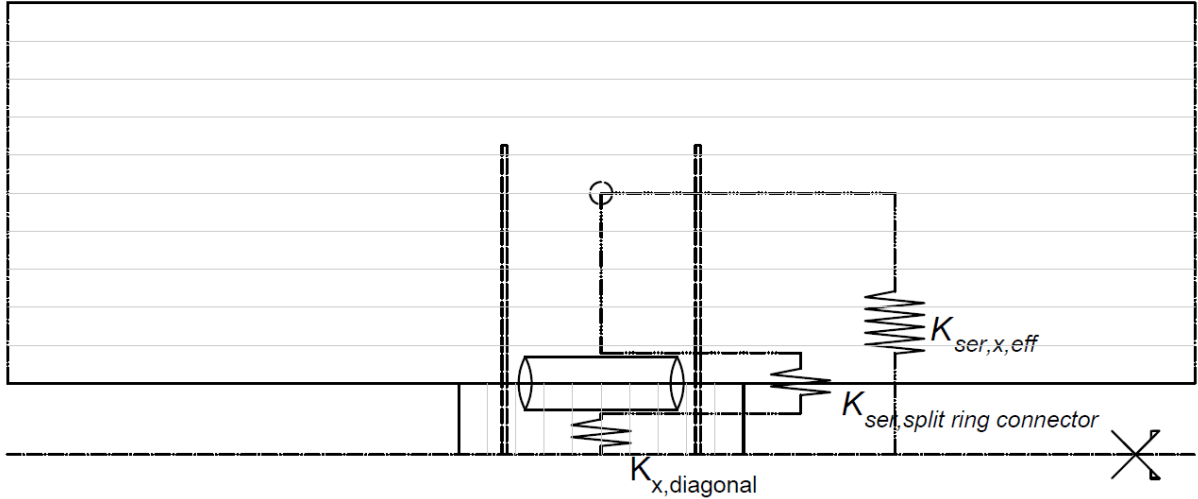
Fig. 21: Representation of the half node with the spring constants for the determination of the shear stiffness

$$K_{ser,eff} = \cfrac{1}{\cfrac{1}{K_{ser,\text{split ring connector}}} + \cfrac{1}{K_{x,diagonal}}}. \tag{9}$$

Fig. 21 presents schematically the serial interaction of both stiffness contributions.

Inserting the density-dependent slip moduli according the Eqs. (4a, b) and the shear stiffness derived in equation (8) one obtains

$$K_{ser,x,eff,\rho_{nom}} = \cfrac{1}{\cfrac{1}{29440} + \cfrac{1}{64320}} = 20196 \; \frac{N}{mm} \quad \text{and} \tag{9a}$$

$$K_{ser,x,eff,\rho_{test}} = 18701 \; \frac{N}{mm} \tag{9b}$$

6.3 Shear stiffness in y-direction of the connection

For the shear stiffness in the y-direction, the shear distortion of the diagonal is neglected. This is justified by the fact that the shear rigidity of the diagonal is almost equal to G_0 and this almost 10 times higher effect as in case of shear stiffness in x-direction is of very little influence.

This results in a stiffness for each shear plane 1 and 2 exclusively bound to the split ring connector of

$$K_{ser,y,eff,\rho_{nom}} = K_{ser,\rho_{nom}} = 29440 \; \frac{N}{mm} \quad \text{and} \tag{10a}$$

$$K_{ser,y,eff,\rho_{test}} = K_{ser,\rho_{test}} = 26368 \ \frac{N}{mm}. \tag{10b}$$

6.4 Rotational stiffness K_{M_y} and K_{M_x} of the connection

The moment resistance, developed by the screw pairs is relevant in terms of basic mechanics. In order to determine the rotational stiffness of the joint, the axial displacement of the screws is needed. The axial displacement is composed of two contributions. First, the slip of the embedded screw in the girder and further the elongation of the screw in the diagonal. For this purpose, the individual screw is divided into two sections, symmetric to the mid plane of the joint (mid plane is dotted line in Fig. 22). Section 1 is the embedded length of the screw in each of the girders, with a slightly different length of $l_{ef} = 200$ mm and 210 mm, respectively. Section 2 is the length of the screw in half of the diagonal. In section 2, the pure elongation of the screw shaft is used to determine the displacement modulus.
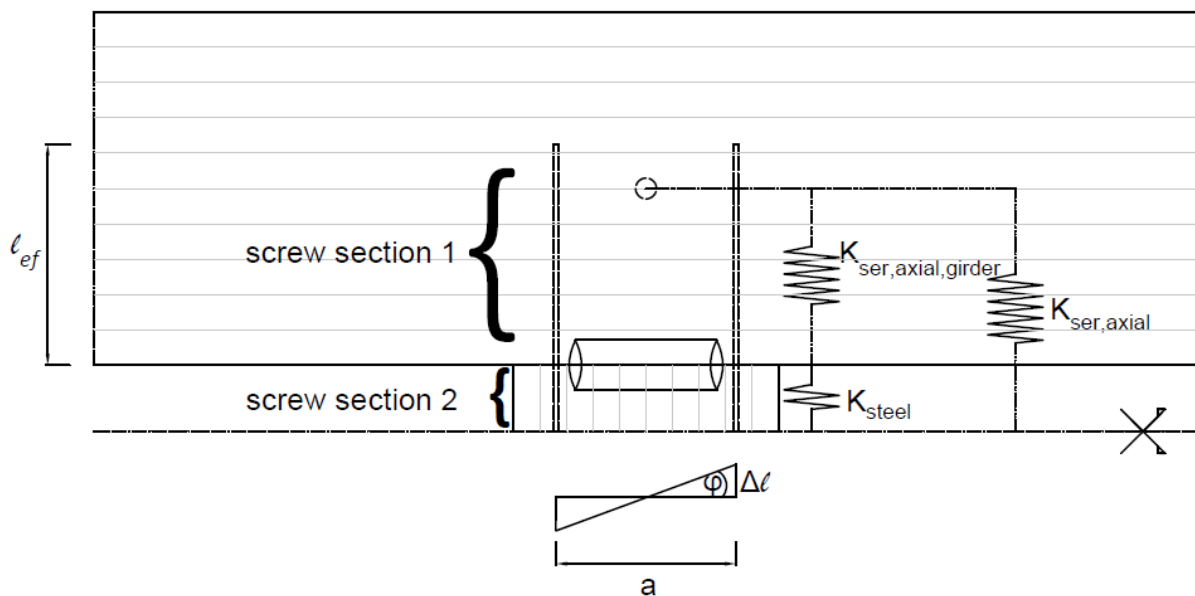
Fig. 22: Representation of half of the node connection (one girder plus half of the diagonal) with the spring constants for the determination of the rotational stiffness

Screw section 1: Axial withdrawal or slip of the screws

In accordance with European Technical Assessment ETA-11/0190 [9] the specially employed screw with a diameter of d = 10 mm is characterised by a slip modulus for the serviceability states of

$$K_{ser,axial,girder} = 25 \cdot d \cdot l_{ef} \tag{11}$$

resulting in

$$K_{ser,axial,girder} = 25 \, \frac{N}{mm^3} \cdot 10 \, mm \cdot 200 \, mm = 50000 \, \frac{N}{mm} \tag{11a}$$

Screw section 2: Elongation of the steel

The calculation of the screw elongation is based on the shaft diameter of the screw $d_s = 7.2$ mm which delivers

$$K_{Steel} = \frac{E \cdot A}{L} = \frac{210000 \frac{N}{mm^2} \cdot \frac{\pi \cdot 7.2 \, mm^2}{4}}{60 \, mm} = 142503 \, \frac{N}{mm} . \tag{12}$$

Finally, the total axial stiffness of the screw is obtained by serial connection of sections 1 and 2a, resulting in

$$K_{ser,axial} = \frac{1}{\frac{1}{K_{ser,axial,girder}} + \frac{1}{K_{Steel}}} = \frac{1}{\frac{1}{50000} + \frac{1}{142503}} = 37013 \, \frac{N}{mm} . \tag{13}$$

Rotational stiffness of the grid joint

The rotational stiffness about the y- and x-axes is defined by the axial stiffness of the screws and the lever arm between the screws. Since there are two pairs of screws, the stiffness is multiplied by a factor of 2. The rotational stiffnesses $K_{M_y} = K_{M_x}$ are derived as follows:

$$F = K_{ser,axial} \cdot \Delta l \, , \tag{14}$$

$$M = F \cdot a = K_{ser,axial} \cdot \Delta l \cdot a \, , \tag{15}$$

$$\varphi = \tan \varphi = \Delta l / (a/2) \, , \tag{16}$$

$$K_{M_y} = K_{M_x} = \frac{M}{\varphi} = 2 \cdot \frac{K_{ser,axial} \cdot a^2}{2} = \frac{37013 \cdot 163^2}{2} = 983.4 \, kNm/rad \, . \tag{17}$$

6.5 Comparison with experimental results

In the following, the calculated stiffnesses are compared with those determined from the experiments. Regarding the comparison of the empiric and calculated results, it should be recalled that the experimental stiffnesses were measured for the entire grid joint and for the individual shear planes (sub joints). Tables 5 to 8 contain the results of the empiric and experimental stiffnesses discussed below.

Table 5: Shear stiffness in x-direction of the connection

calculated shear stiffness one shear plane [kN/mm]		experimental shear stiffness one shear plane [kN/mm]	
$K_{ser,x,eff,\rho_{nom}}$	$K_{ser,x,eff,\rho_{test}}$	$K_{F_{x,1}}$ shear plane 1	$K_{F_{x,2}}$ shear plane 2
20.20	18.70	23.45	20.69

Table 6: Shear stiffness in y-direction of the connection

calculated shear stiffness both shear planes [kN/mm]		experimental shear stiffness both shear planes [kN/mm]
$K_{ser,y,eff,\rho_{nom}}$	$K_{ser,y,eff,\rho_{test}}$	K_{F_y}
58.88	52.74	56.55

Table 7: Rotational stiffness about the y-axis of the connection

calculated rotational stiffness one sub joint [kNm/rad]	experimental rotational stiffness one sub joint [kNm/rad]	
K_{M_y}	joint 1 $K_{M_{y,1}}$	joint 2 $K_{M_{y,2}}$
983.4	3197.2	3920.1

Table 8: Rotational stiffness about the x-axis of the connection

calculated rotational stiffness one sub joint [kNm/rad]	experimental rotational stiffness one sub joint [kNm/rad]	
K_{M_x}	joint 1 $K_{M_{x,1}}$	joint 2 $K_{M_{x,2}}$
983.4	3006	1829

It is apparent that the experimental and calculated shear stiffnesses in x- and y-direction agree very well. In average of shear plane 1 and 2, the experimental value $K_{F,x}$ is 22,07 kN/mm and hence roughly 10 % and 20 % higher as compared to the calculated values depending on either nominal or effective density. In case of shear stiffness in y-direction an even better agreement with rather small differences of 4 % and 7 % can be observed.

In contrast hereto, significant differences between calculated and measured values have to be noted in case of the rotational stiffnesses. In both axes the empiric rotational stiffnesses are in average 2.5 to 3.5 times higher than the calculated results. The pronounced discrepancy and the significantly higher experimental values are most probably bound the following reasons. The angle φ used for the rotational stiffness (Eq. 16) has been determined by a straightforward engineering approach taking the displacement at the tension and compression side divided by the lever arm of the screws. It is well perceivable that the displacement u_2 of the compressed screw of the joint is much less activated and that the angle φ is widely determined by the elongation / slip of the tension stressed screw. In the experiments actually displacements u_2 (compressive side) were throughout much smaller as compared to u_3 (tension side); compare Figs. 14 and 15. This would lead in the extreme case ($u_2 = 0$) to a two times higher calculated rotational stiffness and the difference to the empiric values would reduce to a factor of 1.5 to 2. With this approach, the center of rotation would not be the center of the node, and consequently the internal threaded bolt of the joint should also have a significant effect on the rotational stiffness of the entire grid shell node. This is supported by experimental result that the center bolt is significantly s-shaped bent proving that the bolt represents a significant rotational resistance and hence contributes to the rotational stiffness.

A further reason of the higher empiric stiffness could result from the disregarded impact of the split ring connector, which probably contributes to the rotational stiffness, too, when twisted versus the horizontal axis. In order to assess the theoretical rotational stiffness of the joint more accurate as done above with a straight-forward engineering approach, a 3D finite element analysis should be conducted. In ongoing analysis of the grid shell, it is evaluated to what extent the differences of the rotational stiffnesses affect the stresses and displacements of the whole structure. Depending hereon, eventually a refined analysis and further tests are necessary.

Concluding, it should also be mentioned that the stiffnesses in the tests decreased significantly with an increased number of loading cycles. Hence, the system becomes significantly softer after initial loads, e.g. during the assembly and service time of the structure.

7.   ACKNOWLEDGEMENTS

REFERENCES

[1]   RAIGEL, L.: *Konstruktion von weitgespannten Holzgitterschalen mit besonderer Berücksichtigung von Anschlüssen - Literaturrecherche und Versuche.* Bachelor thesis, Institute for Materials in Building Construction, University of Stuttgart, 2021

[2]   LI, J.: *Timber Shell Structures - Form-finding and structural analysis of actively bent grid shells and segmental plate shells.* PhD thesis, Institute of Building Structures and Structural Design, University of Stuttgart, 2017

[3]   EN 1995-1-1:2004+AC:2006+A1:2008: Eurocode 5: *Design of timber structures – Part 1-1: General-Common rules and rules for buildings.* European Committee for Standardization (CEN), Brussels, Belgium

[4]   EN 408:2010+A1: *Timber structures - Structural timber and glued laminated timber - Determination of some physical and mechanical properties.* European Committee for Standardization (CEN), Brussels, Belgium

[5]   EN 789:2004: *Timber structures – Test methods Determination of mechanical properties of wood-based panels.* European Committee for Standardization (CEN), Brussels, Belgium

[6]   EN 26891:1991: *Timber structures - Joints made with mechanical fasteners - General principles for the determination of strength and deformation characteristics.* European Committee for Standardization (CEN), Brussels, Belgium

[7]   EN 14358:2016: *Timber structures - Calculation and verification of characteristic values.* European Committee for Standardization (CEN), Brussels, Belgium

[8]   HANKINSON, R.L.: *Investigation of crushing strength of spruce at varying angles of grain.* Air Force Information Circular No. 259, U. S. Air Service, 1921

[9]   EUROPEAN TECHNICAL ASSESSMENT ETA-11/0190: *Self-tapping screws for use in timber constructions.* Deutsches Institut für Bautechnik, Berlin, 2018